

Drift Due to Two Obstacles in Different Arrangements

Sergei Melkounian¹ and Bartosz Protas²

¹School of Computational Science and Engineering,
McMaster University
Hamilton, Ontario L8S4K1, CANADA

²Department of Mathematics & Statistics,
McMaster University
Hamilton, Ontario L8S4K1, CANADA

December 8, 2024

Abstract

We study the drift induced by the passage of two cylinders through an unbounded extent of inviscid incompressible fluid under the assumption that the flow is two-dimensional and steady in the moving frame of reference. The goal is to assess how the resulting total particle drift depends on the parameters of the geometric configuration, namely, the distance between the cylinders and their angle with respect to the direction of translation. This problem is studied by numerically computing, for different cylinder configurations, the trajectories of particles starting at various initial locations. The velocity field used in these computations is expressed in closed form using methods of the complex function theory and the accuracy of calculations is carefully verified. We identify cylinder configurations which result in increased and decreased drift with respect to the reference case when the two cylinders are separated by an infinite distance. Particle trajectories shed additional light on the hydrodynamic interactions between the cylinders in configurations resulting in different drift values. This ensemble of results provides insights about the accuracy of models used to study biogenic mixing.

Keywords: Drift; Wakes; Complex Function Theory

1 Introduction

Drift is a phenomenon whereby fluid particles experience a net displacement after the passage of an obstacle in an unbounded domain. It has recently gained renewed attention in the context of mixing in the oceans caused by swimming organisms where drift may play an important role in the overall energy transfer in the oceans [12]. Other applications involve multiphase flows [8] and we refer the reader to our recent study [14] for a survey of the relevant literature. As was initially introduced in the classic studies by Maxwell and Darwin [4, 7], most investigations of drift rely on potential models of flows around a circular cylinder. The effects of wake vortices on drift were investigated in [14] based on the potential flow models of Föppl and Kirchhoff. It was found that, for the Föppl wake model [10], the effect of the wake vortices was to increase the total drift, except for very small wake sizes for which the drift was actually decreased. On the other hand, for the Kirchhoff model [13] the total drift is unbounded.

As regards applications of drift to the studies of mixing, a typical approach [18] is to view the effects of multiple objects as independent of each other, which is equivalent to assuming that the drift induced by the passage of multiple objects is a simple sum of the drifts induced by the individual bodies. In other words, in this approach the geometric nonlinearity of the hydrodynamic interactions is neglected by assuming the drift to be linearly additive. The goal of this study is to address this issue in more detail by considering how the actual drift induced by the passage of multiple objects depends on their geometric configuration. We will do so by focusing on an idealized flow problem in which two identical circular cylinders pass through an unbounded extent of fluid such that their geometric configuration remains unchanged. As a result of this simplification, there are only two parameters in the problem, namely, the distance r between the centers of the obstacles and their inclination, measured by the angle λ , with respect to the direction of motion (Figure 1). Due to symmetry, we will only need to consider the values $0 \leq \lambda \leq \pi/2$. It will be demonstrated that the resulting total drift may be increased or decreased with respect to the linearly additive case depending on the values of the parameters r and λ . The values of the drift obtained in various geometric configurations are correlated with the patterns exhibited by the particle trajectories in the different cases, thereby offering physical insights into the kinematic mechanisms underlying the increase or decrease of drift.

The structure of the paper is as follows: in the next section we define precisely drift and discuss various ways of computing it in general flows; in Section 3 we restrict our attention to two-dimensional (2D) potential flows induced by translating objects; next, in Section 4 we introduce and validate our numerical approach and then in Section 5 we present and discuss the computational results; finally, conclusions are deferred to Section 6.

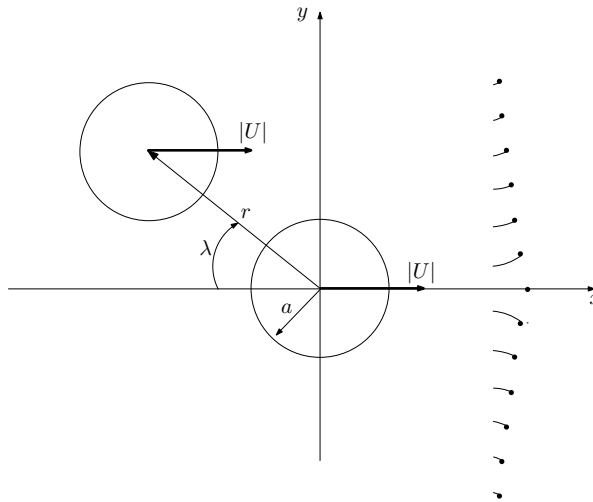


Figure 1: Schematic of the flow configuration at time $t = 0$ in the laboratory frame of reference.

2 Drift: Definition and Calculation

We will consider the motion of N circular cylinders with boundaries Γ_i , $i = 0, 1, \dots, N - 1$, passing through an incompressible inviscid fluid of unit density in a 2D unbounded domain Ω . In our analysis we will use two coordinate systems: one associated with the laboratory frame of reference and the other attached to the moving obstacles (in the latter case we will assume that the cylinder with the boundary Γ_0 has its center at the origin). For a point $(x, y) \in \Omega$, the position and velocity vectors in the laboratory frame of reference will be denoted, respectively, $\mathbf{x} = [x, y]^T$ and $\mathbf{u}(\mathbf{x}) = [u_x, u_y]^T$, where u_x and u_y are the x and y components. It is assumed that the obstacles pass from $x = -\infty$ to $x = \infty$ with a constant speed and in such a way that the distance r between the obstacle centers and the inclination angle λ remain unchanged (Figure 1). In the moving frame of reference, we will denote the position and velocity by $\mathbf{x}' = [x', y']^T$ and $\mathbf{u}'(\mathbf{x}') = [u'_x, u'_y]^T$. It is assumed that in this frame of reference the flow is steady and potential, satisfies the no through-flow boundary condition $\mathbf{u}' \cdot \mathbf{n} = 0$ on each cylinder boundary Γ_i , $i = 0, \dots, N - 1$, and approaches the uniform stream at infinity $\mathbf{u}'(\mathbf{x}') \rightarrow U \hat{\mathbf{x}}'$ as $|\mathbf{x}'| \rightarrow \infty$, where $U = -1$ and $\hat{\mathbf{x}}'$ is the unit vector associated with the x' -axis. We remark that, since the obstacles translate in the direction of the x -axis, the y coordinates in the two coordinate systems coincide ($y \equiv y'$). While the set-up described certainly represents a highly idealized configuration (especially the aspect concerning an infinite passage time), due to the geometric nonlinearity of the problem it allows us to characterize the interactions between obstacles and advected particles at a fundamental level.

Drift is defined in terms of the trajectories of individual particles displaced as the obstacles move through the fluid. Let the initial position of the particle at $t = 0$ be \mathbf{x}_0 and $[x(t; \mathbf{x}_0), y(t; \mathbf{x}_0)]^T$ denote the corresponding particle trajectory for $t < 0$ and $t > 0$.

Then, the drift of the particle initially at \mathbf{x}_0 is defined as

$$\xi(\mathbf{x}_0) := \int_{-\infty}^{\infty} u_x(x(t; \mathbf{x}_0), y(t; \mathbf{x}_0)) dt \quad (1)$$

(the symbol “:=” defines the quantity on the left-hand side with the quantity on the right-hand side). To measure the amount of mixing induced by the obstacles, the quantity that we are most interested in is the *total drift area* D representing the integral displacement of all particles initially located on a line perpendicular to the path of the obstacles at an infinite distance upstream in the moving frame of reference, i.e.,

$$D := \int_{-\infty}^{\infty} \xi(y_\infty) dy_\infty = \int_{-\infty}^{+\infty} \xi(\psi') d\psi', \quad (2)$$

where y_∞ is the transverse coordinate of the particle’s position when $t \rightarrow -\infty$ (which is the same in both coordinate systems) and ψ' is the streamfunction in the moving frame of reference (with a slight abuse of notation, ξ may be equivalently considered a function of \mathbf{x}_0 , y_∞ or ψ). The two integrals in (2) are equal, because $\psi' \rightarrow y_\infty$ as $x' \rightarrow \infty$ which is a consequence of the far-field boundary condition satisfied by the velocity field. The total drift area D involves two nested improper integrals (in expressions (1) and (2)) and this quantity is well-defined only if the order of integration is as indicated here, i.e., first with respect to time (or, equivalently, the streamwise coordinate) and then with respect to the transverse coordinate [2, 9, 19, 20].

In general, as outlined in [14], there are two effective ways to evaluate the total drift area D numerically. In the first method, one can use a suitably transformed definition formula (2) combined with the particle displacement given in (1). The second method is to evaluate the total drift area by using Darwin’s theorem [7] which stipulates that $D = M$, where M is the added mass and the fluid density is assumed equal to the unity. In the case of a single obstacle ($N = 1$), the added mass can be evaluated as follows [17]

$$M = \oint_{\mathcal{C}} \phi n_x ds, \quad (3)$$

where the contour \mathcal{C} is the boundary of the largest simply-connected region with closed streamlines. Generalization of this approach to the case with multiple boundaries ($N \geq 1$) is straightforward. In the present study we will follow the first approach which was thoroughly validated in [14], as it has the additional advantage of providing the particle trajectories, thereby offering insights about various kinematic mechanisms at play.

From the practical point of view, the most convenient way to evaluate the improper integral (1) is to set the initial particle positions \mathbf{x}_0 at $t = 0$ and then obtain the trajectories by integrating the system

$$\frac{d\mathbf{x}(t)}{dt} = \mathbf{u}(\mathbf{x}(t)), \quad \mathbf{x}(0) = \mathbf{x}_0 \quad (4)$$

forward and backward in time, i.e., for $t \rightarrow \pm\infty$, for different \mathbf{x}_0 . Since in the moving frame of reference the initial particle positions in formula (2) are given for $x' \rightarrow \infty$, they need to be transformed to positions with finite streamwise locations in the laboratory frame, e.g., $\mathbf{x}_0 = [0, y_0]^T$. Since for a particle on a given streamline, the streamfunction ψ' is constant and equal to some C , we have

$$C = \psi'(0, y_0) = \lim_{x' \rightarrow \infty} \psi(x', y_\infty) = y_\infty. \quad (5)$$

Defining $g(y_0) := \psi(0, y_0) = y_\infty$ as the map between the y -coordinates of the particle at $x' = 0$ and at $x' = \infty$, we obtain

$$\frac{dy_\infty}{dy_0} = \dot{g}(y_0), \quad (6)$$

where the dot denotes differentiation, so that (2) becomes

$$\begin{aligned} D &= \int_{-\infty}^0 \xi(\psi') d\psi' + \int_0^{+\infty} \xi(\psi') d\psi', \\ &= \int_{-\infty}^{-1} \xi(g(y_0)) \dot{g}(y_0) dy_0 + \int_{+1}^{\infty} \xi(g(y_0)) \dot{g}(y_0) dy_0. \end{aligned} \quad (7)$$

The upper bound in the first integral on the right-hand side (RHS) in (7) and the lower bound in the second integral are now equal to -1 and $+1$, respectively, because the particle on the streamline with $\psi' = 0$ has the initial coordinate $y_0 = \pm 1$ at $x_0 = 0$. The reason is that the value of the streamfunction on the streamline which in the moving frame of reference coincides with the boundary Γ_0 of the first obstacle may be chosen as $\psi' = 0$.

3 Flow Model

First, in Section 3.1, we will briefly review the potential flow theory for the general case of N cylinders with arbitrary radii and positions. Then, in Section 3.2, we will restrict this description to the case of two identical circular cylinders of unit radius ($a = 1$). This is the case for which we will provide computational results and discussion in the remainder of the paper.

Hereafter, without the risk of confusion, we will interchangeably use the vector and complex notation for various vector quantities. A point $\mathbf{x}' = [x', y']^T$ in the moving frame of reference will therefore also be represented as $z = x' + iy'$, where $i := \sqrt{-1}$, and the fluid velocity $\mathbf{u}'(\mathbf{x}') = [u'_x, u'_y]^T$ as $V(z) = (u'_x - iu'_y)(z)$. Since the velocity field is assumed incompressible and irrotational, it will be expressed in terms of the complex potential $W(z) = (\phi' + i\psi')(z)$ as $V(z) = dW/dz$, where ϕ' and ψ' are, respectively, the scalar potential and the streamfunction. Since the flow models are defined in the moving frame of reference, in order to simplify the notation, we will drop the primes from the quantities defined in the complex plane.

3.1 Potential Flows Past Multiple Cylinders

To determine the complex potential and velocity in a flow past multiple cylinders, we apply the methods based on the Schottky-Klein prime function described in [5]. They rely on the definition of suitable conformal maps. The set-up of the problem is such that, in addition to the cylinder with the boundary Γ_0 located at the origin, there are $N - 1$ cylinders with centers and radii denoted $\{Q_j, D_j\}_{j=1}^{N-1}$ in the z -plane and $\{q_j, \delta_j\}_{j=1}^{N-1}$ in the ζ -plane, where $Q_j, q_j \in \mathbb{C}$ and $D_j, \delta_j \in \mathbb{R}$, $j = 1, \dots, N - 1$ (it is assumed that the cylinders have no points of contact). We define a conformal map

$$\zeta(z) = \frac{a}{z - b}, \quad (8)$$

where $a \in \mathbb{R}$ and $b \in \mathbb{C}$ are the radius and position of the cylinder Γ_0 in the z -plane (since for this cylinder we have $a = 1$ and $b = 0$, map (8) simplifies to $\zeta(z) = 1/z$). With this map, we have that the point $\beta = 0$ in the ζ -plane maps to the point $z(\beta) = \infty$ in the z -plane. The relations between the positions and radii of the remaining cylinders in the z and ζ planes are then given by

$$D_j = \frac{\bar{\delta}_j}{|\delta_j|^2 - q_j^2}, \quad (9a)$$

$$Q_j = \frac{q_j}{|\delta_j|^2 - q_j^2}. \quad (9b)$$

Next, for $j = 1, \dots, N - 1$, we define the Möbius maps

$$\theta_j(\zeta) = \frac{a_j \zeta + b_j}{c_j \zeta + d_j}, \quad (10)$$

where

$$a_j = q_j - \frac{|\delta_j|^2}{q_j}, \quad b_j = \frac{\delta_j}{q_j}, \quad c_j = -\frac{\bar{\delta}_j}{q_j}, \quad d_j = \frac{1}{q_j}.$$

Then, the Schottky-Klein prime function is given by

$$\omega(\zeta, \gamma) = (\zeta - \gamma)\tilde{\omega}(\zeta, \gamma), \quad (11)$$

where

$$\tilde{\omega}(\zeta, \gamma) = \prod_{\theta_k} \frac{(\theta_k(\zeta) - \gamma)(\theta_k(\gamma) - \zeta)}{(\theta_k(\zeta) - \zeta)(\theta_k(\gamma) - \gamma)}$$

in which the product is taken over the composition of all possible Möbius maps, called the Schottky group [6]. Function (11) can be evaluated using an algorithm involving a Fourier-Laurent expansion described in [6]. The complex potential characterizing the potential flow past a system of N cylinders subject to the no through-flow boundary conditions imposed on their boundaries is then given by

$$W(\zeta, \beta) = Ua \left(\frac{\partial}{\partial \bar{\gamma}} - \frac{\partial}{\partial \gamma} \right) \log \left[\frac{\omega(\zeta, \gamma)}{|\gamma| \omega(\zeta, \bar{\gamma}^{-1})} \right] \Big|_{\gamma=\beta} \quad (12)$$

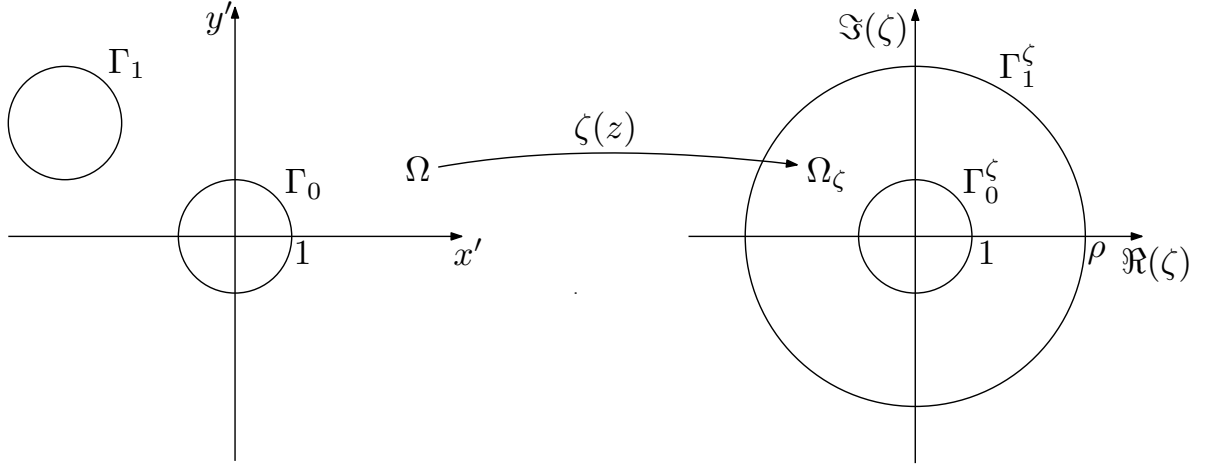


Figure 2: The conformal map (13) from the physical plane z (corresponding to the moving frame of reference) to the ζ plane.

and the corresponding velocity can be computed as $V(z) = (dW/d\zeta)(d\zeta/dz)$. The terms with derivatives with respect to γ , $\bar{\gamma}^{-1}$ and ζ may be computed numerically using finite differences. Alternatively, noting that $\tilde{\omega}(\zeta, \gamma) = \tilde{\omega}(\gamma, \zeta)$, the terms with derivatives with respect to γ and $\bar{\gamma}^{-1}$ may also be computed by differentiating the Fourier-Laurent expansion of $\tilde{\omega}(\gamma, \zeta)^2$, cf. [6].

3.2 Potential Flow Past Two Cylinders

Although it is possible to adopt the techniques from Section 3.1 to find the complex potential for the flow past two cylinders, a simpler formulation is available which involves elliptic functions [11]. In fact, the two approaches are equivalent, since in the case of two cylinders, the complex potential (12) involving the Schottky-Klein prime function reduces to that involving elliptic functions [5]. We start by defining the conformal map

$$\zeta(z) = \frac{\alpha e^{i\lambda} z - 1}{e^{i\lambda} z - \alpha}, \quad (13)$$

where $\alpha = e^\beta$ and $\beta = \cosh^{-1}(-r/2)$. As in [11], the unit cylinder (with boundary Γ_0) located at the origin in the z -plane maps to a unit cylinder at the origin in the ζ -plane (with boundary Γ_0^ζ), cf. Figure 2. The second cylinder Γ_1 is then mapped to cylinder Γ_1^ζ with the center at the origin and with radius $\rho > 1$, where

$$\rho = e^\gamma \quad \text{and} \quad \gamma = \cosh^{-1}[(r^2 - 2)/2].$$

Given the conformal map (13) and defining $\tau := \log \zeta$, the complex potential of the flow past two cylinders becomes

$$W(\tau) = iU \left[e^{-i\lambda} \mathcal{Z}(i(\tau - \beta)) - e^{i\lambda} \mathcal{Z}(i(\tau + \beta)) - \frac{2\mathcal{Z}(\pi) \sin \lambda}{\pi} \tau \right], \quad (14)$$

where $\mathcal{Z} : \mathbb{C} \rightarrow \mathbb{C}$ is the Weierstrass zeta function [16]. To obtain the velocity field $V(z)$, we use the relation $\wp(z) = -\dot{\mathcal{Z}}(z)$, where $\wp : \mathbb{C} \rightarrow \mathbb{C}$ is the Weierstrass P function [16]. Applying the chain rule, we obtain

$$\begin{aligned} V(z) &= \frac{dW}{dz} = \frac{dW}{d\tau} \frac{d\tau}{d\zeta} \frac{d\zeta}{dz}, \\ &= U \left[e^{-i\lambda} \wp(i(\tau - \beta)) - e^{i\lambda} \wp(i(\tau + \beta)) - \frac{2\mathcal{Z}(\pi) \sin \lambda}{\pi} \right] \frac{1}{\zeta} \frac{e^{i\lambda}(1 - \alpha^2)}{(e^{i\lambda}z - \alpha)^2}. \end{aligned} \quad (15)$$

Standard definitions of the special functions \mathcal{Z} and \wp are given below [16]: if ν_1 and ν_2 are nonzero complex numbers such that $\Im(\nu_2/\nu_1) > 0$, then the set of points $w = 2m\nu_1 + 2n\nu_2$ with $m, n \in \mathbb{Z}$ constitutes a lattice \mathbb{L} with generators $2\nu_1$ and $2\nu_2$. Then, the Weierstrass zeta and P functions are defined as

$$\mathcal{Z}(z) = \frac{1}{z^2} + \sum_{w \in \mathbb{L} \setminus \{0\}} \left[\frac{1}{(z-w)^2} - \frac{1}{w^2} \right], \quad (16a)$$

$$\wp(z) = \frac{1}{z} + \sum_{w \in \mathbb{L} \setminus \{0\}} \left(\frac{1}{z-w} + \frac{1}{w} + \frac{z}{w^2} \right), \quad (16b)$$

respectively. Following [11], we set the half-periods to be $\nu_1 = \pi$ and $\nu_2 = i\gamma$, so that we have for $j = 1, 2$,

$$\begin{aligned} \mathcal{Z}(z + 2\nu_j) &= \mathcal{Z}(z) + 2\mathcal{Z}(\nu_j), \\ \wp(z + 2\nu_j) &= \wp(z) \end{aligned}$$

and thus \mathcal{Z} and \wp are, respectively, a quasi-periodic and periodic functions on the lattice \mathbb{L} . Numerical evaluation of the Weierstrass zeta and P functions using the standard definitions in (16a) and (16b) is impractical, because of the slow convergence of the summations with respect to the lattice points $w \in \mathbb{L} \setminus \{0\}$. An alternate formulation expresses the Weierstrass zeta and P functions in terms of the Jacobi theta functions which have Fourier series that do converge rapidly [16]. For some given $q = e^{i\pi\nu_2/\nu_1}$, we then have

$$\mathcal{Z}(z) = \frac{\pi}{2\nu_1} \frac{d \ln \theta_1(\pi z / (2\nu_1), q)}{d(\pi z / (2\nu_1))} - \frac{\pi^2}{12\nu_1^2} \frac{\ddot{\theta}_1(0, q)}{\dot{\theta}_1(0, q)} z, \quad (17a)$$

$$\wp(z) = \left[\frac{\pi \theta_3(0, q) \theta_4(0, q) \theta_2(\pi z / (2\nu_1), q)}{2\nu_1 \theta_1(\pi z / (2\nu_1), q)} \right]^2 + \frac{\pi^2}{12\nu_1^2} (\theta_2^4(0, q) + 2\theta_4^4(0, q)), \quad (17b)$$

where the Jacobi theta functions θ_j , $j = 1, 2, 3, 4$, are given by the Fourier series

$$\theta_1(z, q) = 2 \sum_{n=0}^{\infty} (-1)^n q^{(n+\frac{1}{2})^2} \sin((2n+1)z), \quad (18a)$$

$$\theta_2(z, q) = 2 \sum_{n=0}^{\infty} q^{(n+\frac{1}{2})^2} \cos((2n+1)z), \quad (18b)$$

$$\theta_3(z, q) = 1 + 2 \sum_{n=1}^{\infty} q^{n^2} \cos(2nz), \quad (18c)$$

$$\theta_4(z, q) = 1 + 2 \sum_{n=1}^{\infty} (-1)^n q^{n^2} \cos(2nz). \quad (18d)$$

The derivative terms $\dot{\theta}_1$ and $\ddot{\theta}_1$ appearing in (17a) may be computed by differentiating (18a). For points z in the parts of the domain Ω that we are interested in, the expansions (18a)–(18d) for the Jacobi theta functions typically require only a small number of terms to converge to within the machine precision and are therefore well-suited for numerical evaluation. Using this formulation, we may now compute the Weierstrass zeta and P functions in (17a)–(17b) and use them to evaluate the complex potential and velocity in (14) and (15).

4 Computational Approach

In this section we present and validate the computational approach used to evaluate the total drift area (7) for different geometric configurations. Numerical computation of particle trajectories and the corresponding drift is performed in a similar manner to the approach described in detail in [14]. That is, we solve system (4) with different initial data $\mathbf{x}_0 = [0, y_0]^T$, where $|y_0| > 1$. The velocity $\mathbf{u}(\mathbf{x})$ on the RHS of (4) is obtained in the complex form using formula (15) transformed to the fixed frame of reference, where the Weierstrass zeta and P functions are evaluated using the Jacobi theta functions as described in Section 3.2. We then integrate (4) using MATLAB's `ode113` routine. Integral (1) describing the total displacement of a particle is an improper one and hence requires truncation at some suitably large $t = \pm T$. While the numerical approximation of the integral is declared converged for values of time t when the velocity magnitude drops below the machine precision ϵ , i.e., as soon as $|\mathbf{u}(\mathbf{x}(t))| < \epsilon$, to be on the safe side, we set the maximum integration time T to `realmax` = $\mathcal{O}(10^{300})$, which is the largest number representable in the double precision. In order to ensure suitable accuracy of the time-stepping, the absolute and relative tolerance of the numerical integration performed by the `ode113` routine were selected as `RelTol` = `AbsTol` = 10^{-13} .

In computing the velocity $\mathbf{u}(\mathbf{x})$ there exist round-off errors due to finite-precision arithmetic. The element of our approach which is the most susceptible to these errors is the evaluation of the special functions in (17a)–(17b). However, the impact of these

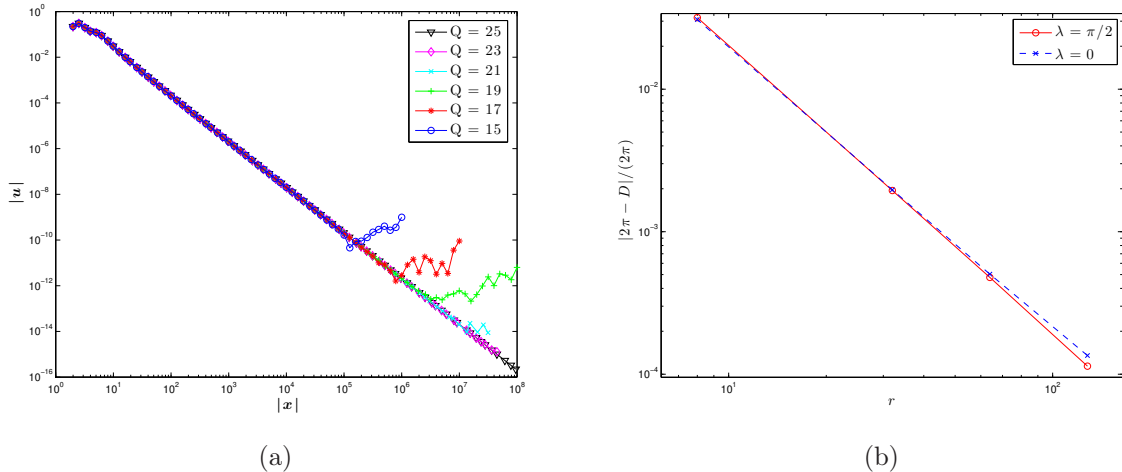


Figure 3: Validation of the computational approach: (a) dependence of $|\mathbf{u}([x, 0]^T)|$ on x with round-off errors becoming more evident as the arithmetic precision is reduced (the numbers of significant digits Q , used in the computations are indicated in the legend), (b) normalized difference between the total drift area induced by two cylinders separated by the distance r and twice the drift of a single cylinder as a function of the separation r .

errors can be controlled by performing the computations with an increased arithmetic precision which in the present study is achieved by using the Advanpix Multiprecision Computing Toolbox for MATLAB [1]. The effect of using different arithmetic precisions on the round-off errors in the evaluation of velocity is illustrated in Figure 3a, where we show the dependence of $|\mathbf{u}([x, 0]^T)|$ when the position of the obstacles is fixed at $t = 0$ on the streamwise coordinate x for x ranging over several orders of magnitude. From the potential flow theory we know that, in the absence of circulation, $|\mathbf{u}(\mathbf{x})| \sim |\mathbf{x}|^{-2}$ as $|\mathbf{x}| \rightarrow \infty$ which is what is indeed observed in Figure 3a for intermediate values of x . For large values of x we detect deviations from this asymptotic behavior due to round-off errors which are however reduced when the arithmetic precision is refined. By performing a number of tests it was determined that the arithmetic precision involving $Q = 25$ significant digits was sufficient to ensure the accuracy of the drift evaluation required for the present study.

Calculation of the total drift area based on formula (7) is implemented as described below. Since the integrals in (7) are improper, there are two steps required to approximate them, namely, truncation of the unbounded integration domain (in the variable y_0) and discretization of the resulting definite integrals with quadratures. As regards the first step, we have the following two possibilities, depending on the location of the second cylinder (with the boundary Γ_1) relative to the y -axis at time $t = 0$:

- if the second cylinder *does not* intersect the y -axis (Figure 4a), the integration domain $[-\infty, -1] \cup [1, \infty]$ in (7) is replaced with $[-1 - \eta - M, -1 - \eta] \cup [1 + \eta, h + \eta + M]$, where $h := r \sin \lambda$, $M > 0$ is a large number and $\eta > 0$ is a small number (introduced to ensure that the initial particle positions do not coincide with the

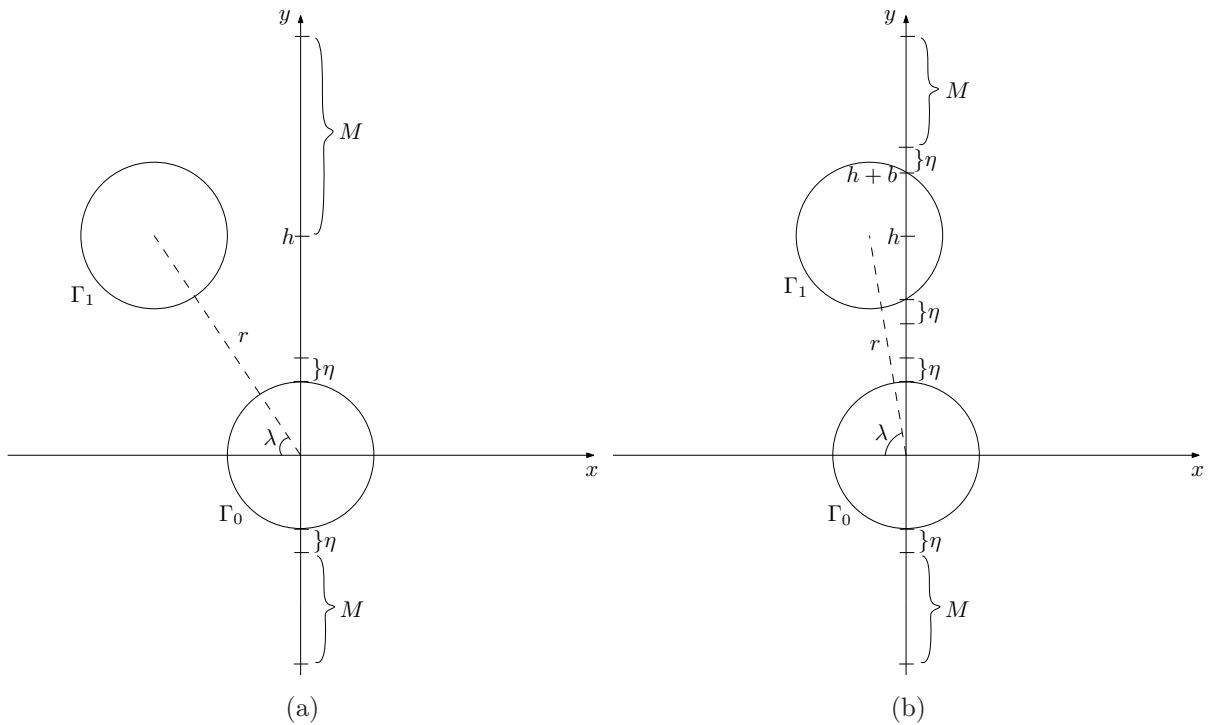


Figure 4: Interpretation of the numerical parameters used in the approximation of integrals in (7) when the second cylinder (a) does not intersect the y -axis and (b) intersects the y -axis at time $t = 0$. The distances corresponding to η and M are not drawn to scale.

obstacle boundary Γ_0 which would lead to numerical difficulties in solving (4),

- if the second cylinder does intersect the y-axis (Figure 4b), the integration domain in (7) is split into *three* parts $[-1 - \eta - M, -1 - \eta] \cup [1 + \eta, h - b - \eta] \cup [h + b + \eta, h + b + \eta + M]$, where $b := \sqrt{1 - r^2 \cos^2 \lambda}$.

In the computations presented below we used $\eta = 10^{-8}$ and $M = 200$ which were found to ensure the required accuracy of the total drift area. The definite integrals obtained as a result of this domain truncation were then approximated using trapezoidal quadratures with the grid (in y_0) selected in such a way that the relative difference of $\xi(y_0)$, cf. (1), corresponding to two adjacent quadrature points did not exceed 1%. To find the function $\dot{g}(y_0)$ appearing in (7), we used the property of potential flows that $u'_x = \Re(V) = \partial\psi'/\partial y$, so that we obtained, cf. (5)–(6),

$$\dot{g}(y_0) = \frac{dy_\infty}{dy_0} = \frac{d\psi'(0, y_0)}{dy_0} = \frac{\partial\psi'(x', y)}{\partial y} \Big|_{x'=0, y=y_0} = \Re(V(z)) \Big|_{z=iy_0} \quad (19)$$

which can be easily evaluated.

To validate the entire numerical approach, we benchmark our computations against a test case when the cylinder separation r is very large. In this limit the exact result is known, because when separated by an infinite distance, the two cylinders do not interact and the total drift area is twice the drift induced by an individual obstacle which is $D_0 = \pi$. Thus, we have $D \rightarrow 2\pi$ as $r \rightarrow \infty$. Figure 3b shows the results of this test performed for the tandem ($\lambda = 0$) and transverse ($\lambda = \pi/2$) configurations. It is evident from this plot that the total drift area indeed approaches 2π for increasing separations r .

5 Results

In this section we present our computational results, first focusing on the trajectories of individual particles for different cylinder configurations and then studying the resulting total drift areas.

5.1 Individual Particle Trajectories

Individual particle trajectories are studied in order to understand the kinematic mechanisms responsible for the different displacements the particles undergo. We focus on the trajectories of particles with initial positions $\mathbf{x}_0 = [0, y_0]^T$ in the fixed frame of reference for three representative cylinder configurations, namely, the tandem ($\lambda = 0$), angled ($\lambda = \pi/4$) and transverse ($\lambda = \pi/2$) configuration with the cylinder separation $r = 3$ in all cases. The trajectories corresponding to different values of y_0 are shown in Figures 5a,b,c together with the corresponding streamline patterns (in the moving frame of reference). Animated versions of these figures are available as Online Resource 1, 2 and 3 accompanying this paper.

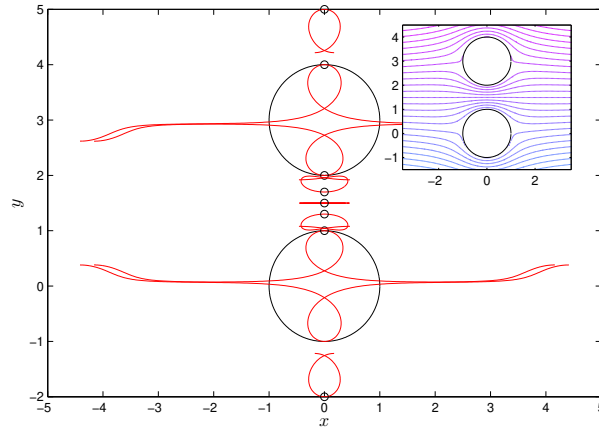
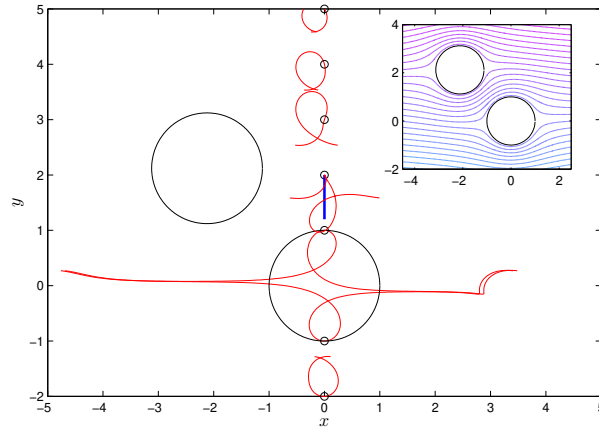
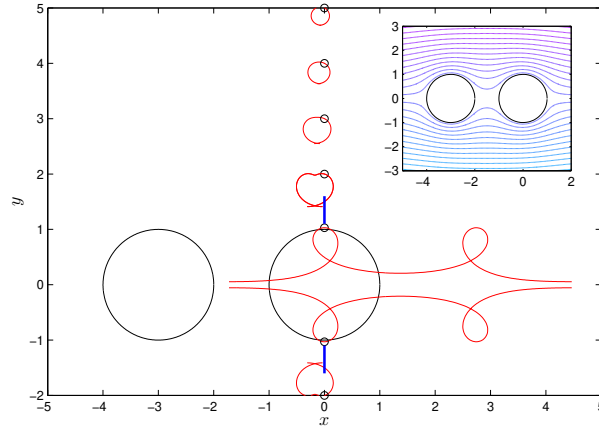
In the tandem configuration in Figure 5a all particle trajectories are symmetric with respect to the flow centerline and we find that the trajectories of the particles passing close to the cylinders exhibit two well defined loops. These trajectories are qualitatively similar to the elastica curves describing the particle trajectories in the single cylinder case [15]. A loop occurs when the particle changes direction as a result of a cylinder passing directly above or below it. Since there are two cylinders, for particles initially close to the flow centerline (i.e., with small $|y_0|$), we observe two such loops, each associated with the passage of one cylinder. On the other hand, for particles further away from the flow axis, the trajectories have only one loop whose shape approaches a circle as $|y_0|$ increases. The range of the initial positions \mathbf{x}_0 for which the trajectories exhibit two loops is marked with a blue solid line in Figure 5a and we find that this range is confined to a region close to the obstacles.

The trajectories of particles in the angled cylinder configuration are shown in Figure 5b. In this case, the vertical symmetry is broken and the trajectories are clearly more complicated. We find that there are again some initial positions \mathbf{x}_0 such that the corresponding trajectories exhibit two loops, however, the trajectories are qualitatively different from those observed in the tandem configuration (Figure 5a). In addition, there is also a range of initial positions \mathbf{x}_0 for which the particles, despite passing very close to Γ_0 , have trajectories which contain only one loop. Furthermore, particles with initial positions close to Γ_0 have trajectories exhibiting a “kink” at large times $t > 0$. This kink occurs at the instant when the second cylinder with the boundary Γ_1 passes from above drawing the particle toward its rear stagnation point. Particles with initial locations further away from the cylinders again show more circular trajectories.

In the transverse cylinder configuration shown in Figure 5c, the vertical symmetry is now restored with the symmetry axis at $y = 1.5$ half-way between the two cylinders. For a particle initially located at $\mathbf{x}_0 = [0, 1.5]^T$, there is no vertical displacement, because the vertical components of the velocity induced by the two cylinders cancel. Regardless of the initial transverse coordinate y_0 , all particles follow trajectories with only one loop which is because their motions are dominated by the cylinder they are closest to.

5.2 Total Drift Area

In this section we present and analyze some global diagnostic quantities characterizing the displacement of the particles depending on the geometric configuration of the two cylinders. We begin by plotting the displacement $\xi(y_\infty)$ of particles located at $[0, y_\infty]^T$ at time $t = -\infty$ as a function of y_∞ for different inclination angles λ in Figure 6 (for consistency with the set-up of the problem, the “independent” variable y_∞ is measured along the vertical axis). The quantity $\xi(y_\infty)$ represents the total distance travelled by a particle initially at y_∞ as the cylinders move from $x = -\infty$ and $x = \infty$, cf. (5)–(6). Formation of the profiles $\xi(y_\infty)$ during the passage of the obstacles is shown for $\lambda = 0, \pi/4, \pi/2$ in Online Resource 1, 2 and 3 accompanying this paper. In Figure 6 we see that $\xi(y_\infty)$ becomes unbounded for certain values of y_∞ which occurs when the corresponding streamline is connected to the front stagnation point on one of the



(c) transverse configuration ($\lambda = \pi/2$)

Figure 5: Particle trajectories for different initial conditions $\mathbf{x}_0 = [0, y_0]^T$ in (a) the tandem, (b) the angled and (c) the transverse cylinder configurations. The symbols \circ denote the particle positions at time $t = 0$ when the cylinders are at the indicated locations. The blue solid lines in (a) and (b) indicate the range of \mathbf{x}_0 for which the trajectories exhibit two loops, whereas the insets show the corresponding streamline patterns in the moving frame of reference.

cylinders (a phenomenon which is well understood in the single cylinder case [3]). The quantity $\xi(y_\infty)$ diverges, respectively, for one and two values of y_∞ when the inclination angle is $\lambda = 0$ or $0 < \lambda \leq \pi/2$, which reflects the number of the front stagnation points facing the flow. In Figure 6 we also observe that as λ increases from 0 to $\pi/2$ the distance between the values of y_∞ for which $\xi(y_\infty)$ diverges increases. We reiterate that the total drift area is obtained by integrating $\xi(y_\infty)$ with respect to y_∞ , cf. (2).

Our main result concerns the dependence of the total drift area D on the horizontal and vertical separation, respectively $r \cos \lambda$ and $r \sin \lambda$, between the two cylinders and this data is shown in Figure 7. Since $r > 2$, this region is left blank in the bottom right corner of the plot. We see that there are two regions in this parameter space corresponding to $D < 2\pi$ and $D > 2\pi$ where the total drift area is, respectively, decreased or increased with respect to twice the drift of a single cylinder. This illustrates how the hydrodynamic interaction of the cylinders due to the geometric nonlinearity of the problem impacts the displacement of the particles. In Figure 7 we see that the total drift area is decreased with respect to the non-interacting reference case with $D = 2\pi$ for small inclination angles λ corresponding to more “streamlined” cylinder configurations, whereas the opposite effect is observed for larger inclination angles. For increasing separation r the border between the regions with $D < 2\pi$ and $D > 2\pi$ approaches a straight line described by $\lambda = \pi/4$. The deviation of the total drift area from the reference value $D = 2\pi$ increases for small separations $r \rightarrow 2$.

It is interesting to find out what are the largest and smallest values of the total drift area which can be attained. This question is addressed in Figure 8 where we show the values of D for $r \rightarrow 2$ in the tandem ($\lambda = 0$) and transverse ($\lambda = \pi/2$) configurations (numerical evaluation of the drift when $r = 2$, i.e., when the two cylinder touch, is not possible due to a singularity of the potential flow formulation, cf. Section 3.2). We see that the largest and smallest drift values are, respectively, $D \approx 2.2 \times 2\pi$ and $D \approx 0.6 \times 2\pi$, and are attained when the two cylinders touch in the transverse and tandem configurations. The increase of the drift in the former case can be understood as being due to the two cylinders creating a “cavity” in front of them which traps particles as the cylinders advance. On the other hand, in the tandem configuration the front stagnation point of the rear cylinder is shielded by the first cylinder which reduces the trapping effect.

6 Discussion, Conclusions and Outlook

In this study we have focused on the drift induced by the passage of two circular cylinders in an unbounded incompressible fluid under the assumptions that the flow is potential and stationary in the moving frame of reference. Knowing that when the two cylinders are separated by an infinite distance, the total drift area is equal to twice the drift induced by one cylinder, the goal was to analyze how the geometric configuration of the cylinders, namely, their separation and inclination with respect to the translation direction, affect the total drift. For each considered configuration, the problem was

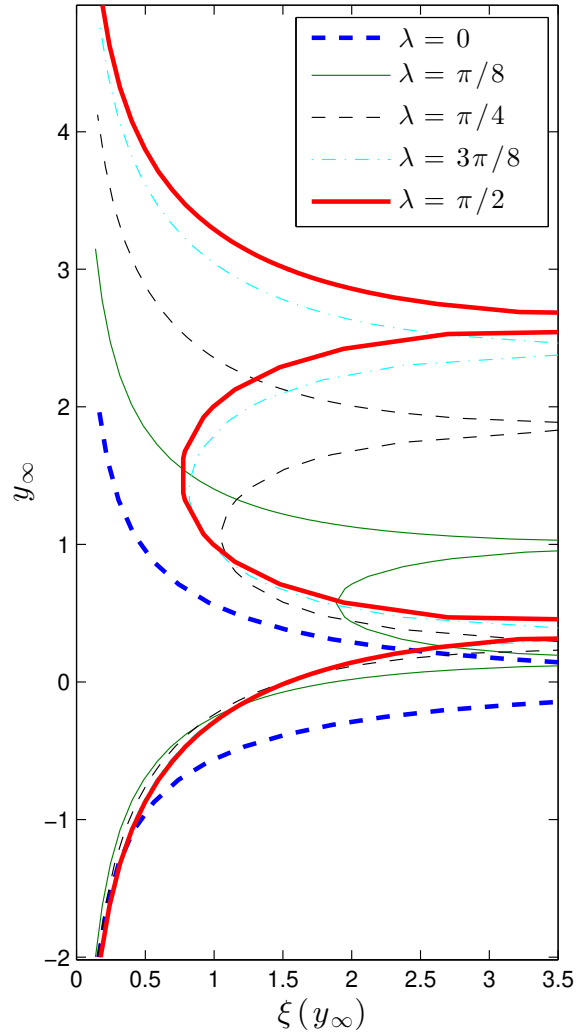


Figure 6: Displacement $\xi(y_\infty)$ of particles located initially (i.e., when $t = -\infty$) at $[0, y_\infty]^T$ as a function of y_∞ for cylinders with different inclination angles indicated in the legend. The separation between the cylinders is $r = 3$.

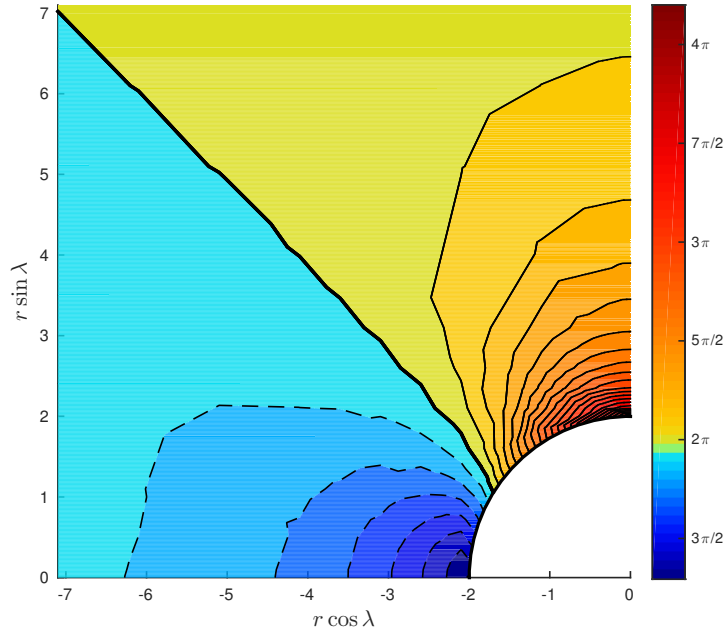


Figure 7: Total drift area D as a function of the horizontal and vertical separation between the two cylinders. The thick solid line corresponds to $D = 2\pi$, whereas the thin dashed and solid lines represent isocontours of D , respectively, in areas where $D < 2\pi$ and $D > 2\pi$.

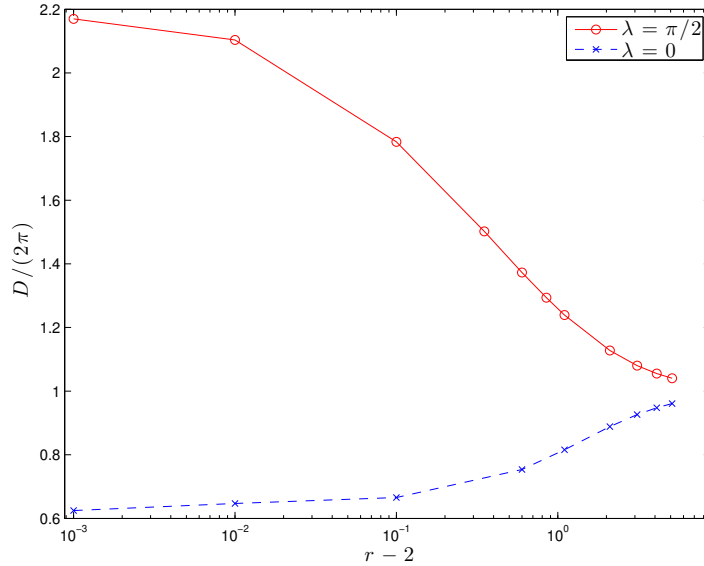


Figure 8: Normalized total drift area D as a function of the separation r between the cylinders in the tandem ($\lambda = 0$) and transverse ($\lambda = \pi/2$) configurations.

studied by integrating particle trajectories numerically with high precision for a range of different initial particle positions. The velocity field induced by the two cylinders during their passage was expressed in closed form in terms of special functions using methods of the complex function theory (cf. Section 3). In contrast to the computation of drift based on Darwin’s theorem, the present approach provides additional information about the shapes of the particle trajectories which sheds light on the kinematic mechanisms responsible for the increase or decrease of the total drift area in comparison with the reference case when the two cylinders are infinitely separated.

While the set-up of our problem is admittedly highly idealized, where we assume an infinite passage time and time-invariance of the geometric configuration, this problem nonetheless offers some fundamental insights into the relation between the flow geometry and drift. We emphasize here that, although the equations governing potential flows are linear in the flow variables, they exhibit a *nonlinear* dependence on the geometry of the flow domain. This nonlinearity is manifested in the results reported in Section 5, which demonstrate that the drift induced by individual obstacles may not be simply added to produce the total drift. More specifically, we showed that for small inclination angles λ , resulting in more “streamlined” cylinder arrangements, the total drift area is decreased in comparison with the reference case, and is increased in configurations characterized by the inclination angle λ larger than $\pi/4$ (cf. Figure 7). We also determined the extreme values attained by the total drift area D which correspond to the vanishing separations between the two cylinders in the tandem and transverse configurations (cf. Figure 8). As regards the particle trajectories obtained in the different configurations, we observed that high-drift cases lead to trajectories with a single loop (cf. Figure 5a), whereas in the low-drift configurations particle trajectories starting at certain initial locations may actually exhibit two loops (cf. Figures 5b,c). The results obtained in the present study may help quantify and improve the accuracy of models used to describe mixing caused by multiple objects in various biological and multiphase flow applications.

Acknowledgements

The authors wish to thank Prof. Takashi Sakajo and Dr. Rhodri Nelson for their advice concerning potential flow models for flows past multiple obstacles. Partial support for this research was provided by an NSERC (Canada) Discovery Grant.

References

- [1] Multiprecision Computing Toolbox for MATLAB 3.8.5.9059. Advanpix LLC., Yokohama, Japan (2015)
- [2] Benjamin, T.B.: Note on added mass and drift. *Journal of Fluid Mechanics* **169**, 251–256 (1986)

- [3] Childress, S.: An Introduction to Theoretical Fluid Mechanics. Courant Lecture Notes in Mathematics. American Mathematical Society, Courant Institute of Mathematical Sciences (2009)
- [4] Clerk-Maxwell, J.: On the displacement in a case of fluid motion. Proceedings of the London Mathematical Society **3**, 82–87 (1870)
- [5] Crowdy, D.: Analytical solutions for uniform potential flow past multiple cylinders. Eur. J. Mech. B/Fluids **25**, 459–470 (2006)
- [6] Crowdy, D.G., Marshall, J.S.: Computing the schottky-klein prime function on the schottky double of planar domains. Computational Methods and Function Theory **7**, 293–308 (2007)
- [7] Darwin, C.: Note on hydrodynamics. Mathematical Proceedings of the Cambridge Philosophical Society **49**, 342–354 (1953)
- [8] Eames, I.: The concept of drift and its application to multiphase and multibody problems. Philosophical Transactions of the Royal Society A: Mathematical, Physical and Engineering Sciences **361**, 2951–2966 (2003)
- [9] Eames, I., Belcher, S.E., Hunt, J.C.R.: Drift, partial drift and Darwin’s proposition. Journal of Fluid Mechanics **275**, 201–223 (1994)
- [10] Föppl, L.: Wirbelbewegung hinter einem Kreiscylinder. *Sitzb. d. k. Bayr. Akad. d. Wiss.* **1**, 1–17 (1913)
- [11] Johnson, E.R., McDonald, N.R.: The motion of a vortex near two circular cylinders. Proceedings of the Royal Society of London A **460**, 939–954 (2004)
- [12] Katija, K., Dabiri, J.O.: A viscosity-enhanced mechanism for biogenic ocean mixing. Nature **460**, 624–626 (2009)
- [13] Levi-Civita, T.: Scie e leggi di reistenza. Rendiconti del Circolo Matematico di Palermo **XXIII**, 1–37 (1907)
- [14] Melkounian, S., Protas, B.: Wake effects on drift in two-dimensional inviscid incompressible flows. Physics of Fluids **26**, 123,601 (2014)
- [15] Milne-Thomson, L.M.: Theoretical Hydrodynamics. Dover (1968)
- [16] Olver, F.W.J., Lozier, D.W., Boisvert, R.F., Clark, C.W. (eds.): NIST Handbook of Mathematical Functions. Cambridge University Press, New York, NY (2010)
- [17] Saffman, P.G.: Vortex Dynamics. Cambridge Monographs on Mechanics and Applied Mathematics. Cambridge University Press, Cambridge (1992)

- [18] Thiffeault, J.L., Childress, S.: Stirring by swimming bodies. *Physics Letters A* **374**, 3487–3490 (2010)
- [19] Yih, C.S.: New derivations of Darwin’s theorem. *Journal of Fluid Mechanics* **152**, 163–172 (1985)
- [20] Yih, C.S.: Evolution of Darwinian drift. *Journal of Fluid Mechanics* **347**, 1–11 (1997)